Photodissociation dynamics of the $A\ ^2\Sigma^+$ state of SH and SD radicals

R. A. Rose,[1] A. J. Orr-Ewing,[1,a)] C.-H. Yang,[2] K. Vidma,[2] G. C. Groenenboom,[2] and D. H. Parker[2]
[1]*School of Chemistry, University of Bristol, Cantock's Close, Bristol BS8 1TS, United Kingdom*
[2]*Institute for Molecules and Materials, University of Nijmegen, Heyendaalseweg 135, 6525 AJ Nijmegen, The Netherlands*

(Received 30 October 2008; accepted 5 December 2008; published online 20 January 2009)

Atomic sulfur products from predissociation of the lowest rotational states of SH/SD $A\ ^2\Sigma^+$ ($v'=0,1,2$) are studied using velocity map imaging. The dissociation process, which is slow compared to rotation, is dominated by interference effects due to predissociation of states with low rotation quantum numbers prepared by photoexcitation using overlapping transitions of different parities. The measured product angular distributions can be modeled using the methods presented recently by Kim *et al.* [J. Chem. Phys. **125**, 133316 (2006)]. The $S(^3P_J)$ (2+1) resonance enhanced multiphoton ionization scheme used in the detection step of the experiment is sensitive to the angular momentum polarization of the atomic fragments. $S(^3P_J)$, $J=2,1,0$, fine-structure yields, angular distributions, and atom polarization parameters are reported. Strong polarization of the $S(^3P_{2,1})$ products was observed along with a weak sensitivity of the branching ratio to excess energy and a full insensitivity of the atomic product polarization to excess energy. None of the data fit the predictions of either adiabatic or diabatic photodissociation, emphasizing the need for a fully quantum treatment. © *2009 American Institute of Physics*. [DOI: 10.1063/1.3056570]

I. INTRODUCTION

The past decade has witnessed tremendous progress in the understanding of the photodissociation of closed-shell diatomic molecules. For the hydrogen halides (H*X*, *X*=F, Cl, Br, I), for example, fully quantum calculations[1,2] combined with advanced imaging experiments[3] have unraveled the intricate dynamics of a molecule evolving from its optically excited molecular orbital configuration to its final product atoms. Using this combined approach of experiment and theory, it is now possible to determine the amplitudes and phases of the fragment matter waves that describe a *complete* photochemical experiment.[4,5]

For a few molecules, fully quantum mechanical calculations are available to guide the interpretation of photodissociation dynamics. For the rest, photodissociation is described by limiting case models based on adiabatic, sudden, or statistical approximations.[6] Detailed investigation of diatomic molecule photodissociation is thus crucial in evaluating the validity of these limiting case models, which are at present the best tools available for interpreting the photodissociation dynamics of complex polyatomic molecules.

Open-shell molecules such as the covalent hydroxyl and mercapto radicals, OH and SH, tend to absorb at longer wavelengths and more readily produce highly reactive fragments such as $O(^1D)$ and $S(^1D)$ than most closed-shell molecules. Owing to their relatively simple electronic structure, a fully quantum treatment of the photodissociation properties of OH (Refs. 7–10) and the isovalent SH (Ref. 11) [and HCl^+ (Ref. 12)] molecules should soon be tractable. Experimentally, however, the production and isolation of sufficient concentrations of these species for further study are challenging. Although OH has been the subject of numerous theoretical and experimental investigations, only a few collision-free studies of OH photodissociation have been reported.[13–15] Velocity map imaging detection of O and H atom products was previously used by Radenovic *et al.* to study direct one-photon photodissociation of vibrationally excited OH and OD $X\ ^2\Pi(v'')$ via the repulsive $1\ ^2\Sigma^-$ electronic state,[13,14] while Zhou *et al.* used H-Rydberg atom photofragment translational spectroscopy (HR-PTS) to study predissociation of OH excited to the $A\ ^2\Sigma^+$ ($v'=3$ and 4) levels.[15]

Reports of the photodissociation dynamics of SH and SD also remain sparse, although the spectroscopy of the SH and SD $A\ ^2\Sigma^+$-$X\ ^2\Pi$ band systems is well explored and understood. In early studies, broadening of spectroscopic lines was observed as the SH($A\ ^2\Sigma^+$) vibrational quantum number increased.[16,17] The line broadening is a consequence of predissociation, which reduces the lifetime of the excited state. Laser induced fluorescence[18–20] and cavity ring-down spectroscopy[21,22] were subsequently used to measure the lifetimes of SH($A\ ^2\Sigma^+, v'=0-2$) and SD($A\ ^2\Sigma^+, v'=0-2$) levels, and their dependence on rotational quantum number (N'). The reductions in lifetimes as v' increases and the N'-level dependence were quantitatively modeled by a series of calculations using *ab initio* and experimentally fitted[21,23,24] potential energy (PE) curves and Fermi golden rule (FGR) calculations. The $A\ ^2\Sigma^+$ state correlates diabatically to $H(^2S)+S(^1D)$ atomic fragments but is crossed by three repulsive PE curves, $1\ ^4\Sigma^-$, $1\ ^2\Sigma^-$, and $1\ ^4\Pi$, that correlate to the ground dissociation limit $H(^2S)+S(^3P)$ as illustrated in Fig. 1. Coupling from the $A\ ^2\Sigma^+$ state to one or more of these repulsive PE curves causes predissociation. The FGR calcu-

a)Electronic mail: a.orr-ewing@bris.ac.uk. Telephone: +44-(0)117-9287672. Fax: +44-(0)117-9250612.

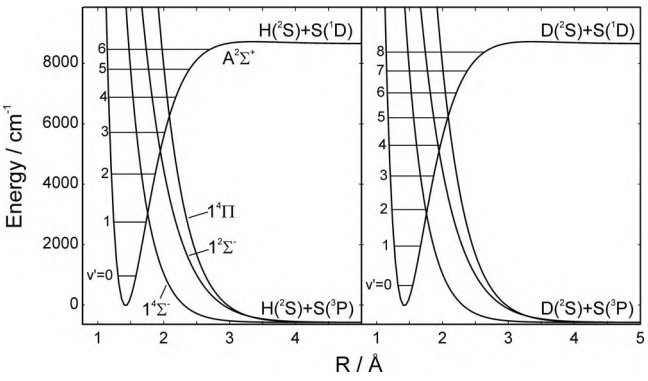

FIG. 1. PE curves for the low-lying excited electronic states of SH and SD [adapted from Wheeler *et al.* (Ref. 21)], with the PE defined relative to the minimum in the bound $A\ ^2\Sigma^+$ state potential. The energies of the vibrational levels of the $A\ ^2\Sigma^+$ state are also shown.

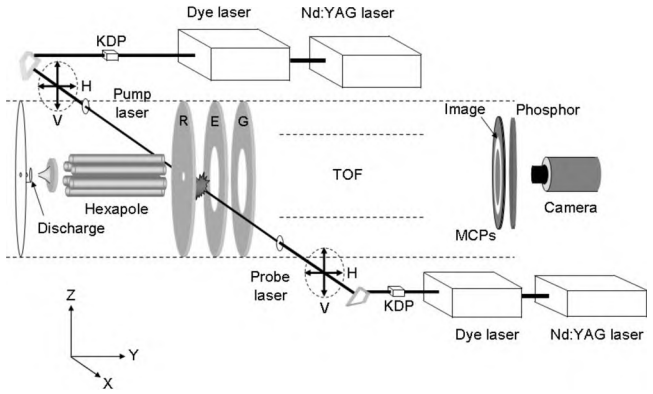

FIG. 2. Schematic of the experimental setup. R, E, and G represent the repeller, extractor, and ground plates of the ion optics, respectively. The polarization directions *H* and *V* of the pump and probe lasers are illustrated and are defined in the main text. TOF represents the time-of-flight tube and MCPs denote microchannel plates. The hexapole device was used only during optimization of the nozzle discharge conditions.

lations by Wheeler *et al.*[21] and later by Brites *et al.*[23] probed the contributions of these couplings to the lifetimes of SH($A\ ^2\Sigma^+, v', N'$) and attributed predissociation of SH($A\ ^2\Sigma^+, v'=0-2$) and SD($A\ ^2\Sigma^+, v'=0-2$) to spin-orbit mediated interactions almost exclusively with the $1\ ^4\Sigma^-_{1/2}$ state; only for higher vibrational levels do couplings to the $1\ ^2\Sigma^-$ and $1\ ^4\Pi$ states become competitive or dominant.

These various spectroscopic and computational studies identified the states participating in the predissociation of low vibrational levels of the $A\ ^2\Sigma^+$ state of SH and SD and provided estimates of the strengths of the couplings between the bound and the dissociative excited states. They did not, however, provide any information on the dynamics that occur following coupling into one or more of the repulsive electronic states: for example, the associated bond breaking may occur adiabatically on a single PE curve or via nonadiabatic transitions between these repulsive states (as is known to arise for HF, HCl, and HBr). Zhang *et al.*[25] used HR-PTS to study direct photodissociation via the $1\ ^2\Sigma^-$ repulsive state, and Dillon and Yarkony undertook computational studies of the dynamics[26] to address these uncertainties. Direct dissociation via the repulsive wall of the bound $A\ ^2\Sigma^+$ state was observed by Janssen *et al.*[27] when starting from $v''=2-6$ vibrational levels of the ground $X\ ^2\Pi$ state and exciting above the H(^2S)+S(^1D) dissociation limit. There have also been analyses of the dynamics of secondary photodissociation of SH radicals produced from H_2S at UV wavelengths ranging from 193 to 244 nm;[28–31] at these wavelengths, excitation of the SH is to one or more repulsive potentials including the $1\ ^2\Sigma^-$ state.

In our previous study of direct SH and SD photodissociation[27] and in the current work, which focuses on predissociation dynamics of the $A\ ^2\Sigma^+$ state at excitation wavelengths from 292 to 324 nm, we employed a pulsed electric discharge supersonic expansion as a source of the mercapto radicals. To derive detailed information about photofragment angle *and* speed distributions, we used the velocity map imaging technique, coupled with polarized laser photodissociation and resonance enhanced multiphoton ionization (REMPI) detection of $S(^3P_J)$ photofragments. The predissociation of mercapto radicals that have been selectively prepared in specified rovibrational levels of the $A\ ^2\Sigma^+$ excited electronic state occurs on a time scale comparable to the rotational period. Under such circumstances, the spatial anisotropy of the internuclear axis in the transient excited state varies with the rotational transition due to interference effects,[32,33] and therefore so does the space-fixed recoil anisotropy. By measuring values of the anisotropy parameter β_v across several rovibrational transitions, detailed insights are obtained of the dissociation in the molecular frame. Nuclear spin angular momentum can also couple to the prepared rotational and electronic angular momenta of the excited state through hyperfine interactions on the time scale of the experiment, potentially affecting the measured angular distributions. Furthermore, the energy splitting of the e,f parity states of the SH free radical is sufficiently small that there is simultaneous excitation of different parity states, leading to a second level of interference effects, which can be simulated, together with the effects of molecular rotation, using the treatment by Houston and co-workers.[32,34] From velocity map images, resolved at the $S(^3P_J)$ spin-orbit level, and their dependence on the polarization of the probe laser, we derive anisotropy parameters, $S(^3P_J)$ spin-orbit branching ratios, and *m*-state propensities. The outcomes of these measurements enable us to make detailed deductions about the dynamics on coupled, dissociative PE curves that cross the $A\ ^2\Sigma^+$ state and correlate to H(^2S)+S(^3P) photofragments.

II. EXPERIMENTAL

A detailed description of our velocity map imaging apparatus has been given in previous publications,[13,14,27,35] and a schematic is presented in Fig. 2. In short, a mixture of 25%–30% H_2S (D_2S) in Xe was expanded into a vacuum chamber through a pulsed (10 Hz) Jordan valve (0.5 mm orifice diameter) and a pulsed ring-type stainless-steel discharge electrode (4 mm diameter).[36] The pulsed-discharge electrode was mounted 2 mm downstream from the valve orifice, and SH (SD) radicals were produced in the discharge during the supersonic expansion. The voltage and the width and delay of the pulse applied to the discharge device were optimized for the expansion conditions (~2 bar backing

pressure behind the nozzle) by monitoring 2+1 REMPI signals of SH (SD) radicals.[37] For the most stable working condition, the discharge device was operated at ~2 kV. Downstream, the SH (SD) beam was collimated by a skimmer (diameter=1 mm) and the 4 mm diameter aperture of the repeller plate of the ion optics assembly; these collimation apertures were situated 15 and 210 mm, respectively, from the pulsed valve. A 120 mm long electrostatic hexapole lens, situated in between the skimmer and repeller plate, was used to state select and focus the SH (SD) beam ($J=3/2$, $|M_J|=3/2$, upper Λ doublet state)[38] to increase the SH (SD) REMPI signals, and thus to aid optimization of the discharge conditions. The slow ~300 m/s SH (SD) beam speed produced by seeding the precursor (H_2S or D_2S) in Xe carrier gas was necessary for hexapole focusing. During the experimental measurements of SH (SD) predissociation, the hexapole was always turned off so there was no initial state selection of the radicals. The SH (SD) beam was directed along the axis of a time-of-flight (TOF) tube and crossed at right angles by the counterpropagating pump (photolysis) and probe (ionization) laser beams, with the region of intersection lying between the repeller and extractor velocity mapping electrodes. The point of photolysis/ionization was positioned about 220 mm from the valve orifice. When the valve was operating, the pressure was $\sim 10^{-4}$ mbar in the source chamber and $\sim 10^{-7}$ mbar in the ionization chamber.

The linearly polarized pump and probe laser beams were focused by $f=20$ and 11 cm focal length lenses, respectively. The focal points of two lasers were shifted ~0.5 cm away from the center of the SH (SD) beam to avoid saturation and power-broadening problems. The time delay between the two laser pulses was less than 10 ns. As depicted in Fig. 2, the vertical (V) polarization direction of the lasers is taken to be perpendicular to the TOF direction and parallel to the detector [microchannel plate (MCP)] face. The direction of horizontal (H) polarization is parallel to the TOF direction and perpendicular to the plane of the detector. Rotation of the polarizations between V and H polarizations for both lasers was carried out using separate zero-order phase retardation plates. The ~292–324 nm pump-laser radiation (0.8–1.5 mJ/pulse, ~0.6 cm^{-1} linewidth), which excites the $A\ ^2\Sigma^+\ (v'=0-2,N') \leftarrow X\ ^2\Pi_{3/2}(v'=0,N'')$ one-photon transitions,[9,10,16,17] was generated by frequency doubling (with a potassium dihydrogen phosphate (KDP) crystal) the output of a dye laser (Spectra Physics Quanta Ray PDL-2) pumped by the second harmonic of a neodymium doped yttrium aluminum garnet (Nd:YAG) laser (Quanta Ray DCR-3). $S(^3P_{2,1,0})$ atom products from predissociation of SH (SD) were ionized by a (2+1) REMPI process via the $3s^23p^3(^4S^o)4p$ state using a probe laser wavelength of ~308–311 nm.[39] This probe radiation (2 mJ/pulse; ~0.6 cm^{-1} linewidth) was generated by frequency doubling (also with a KDP crystal) the fundamental light from a dye laser (Spectra Physics Quanta Ray PDL-2) pumped by the second harmonic of a Nd:YAG laser (Quanta Ray GCR). In order to check the REMPI detection efficiencies for $S(^3P_J)$ spin-orbit levels with $J=0$, 1, and 2, a third laser system was used to photolyze SH via the $1\ ^2\Sigma^- \leftarrow X\ ^2\Pi$ excitation at wavelengths of 226 and 232 nm. The measured branching ratios at these UV wavelengths were compared with the results of Zhou *et al.*[25] Frequency doubling (in a β-barium borate crystal) the output of a Nd:YAG-pumped dye laser (Continuum Surelite and Spectra Physics Quanta Ray PDL-2) was used to generate the 226 and 232 nm wavelengths required. The wavelengths and linewidths of all laser systems were calibrated and measured by a wavelength meter (High Finesse, WS-7).

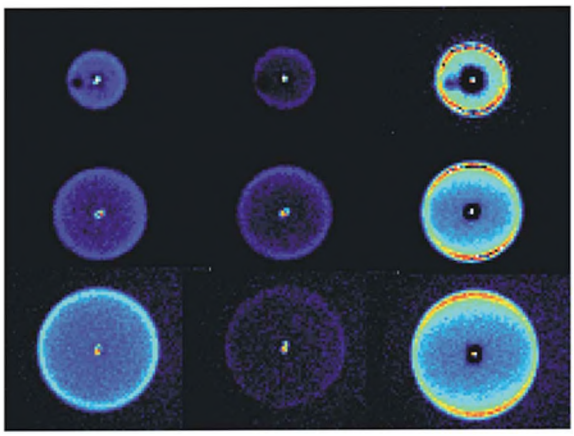

FIG. 3. (Color online) Raw velocity map images of $S(^3P_J)$ from SH photodissociation via $SH(A,v=0)$ (top), $SH(A,v=1)$ (middle), and $SH(A,v=2)$ (bottom). Images shown in the columns from left to right are for $S(^3P_J)$ with $J=0$, 1, and 2.

$S(^3P_J)$ ions formed by the REMPI process were extracted from the ionization region into the grounded TOF tube by an electrostatic velocity mapping lens and crushed onto a two-dimensional (2D) MCP and phosphor-screen detector monitored by a charge coupled device camera. Mass selectivity was achieved by pulsing (~100 ns duration) the gain of the MCPs as the S^+ ($m/z=32$) ions arrived. The flight distance of S^+ ions was ~385 mm from the point of ionization to the front plate of the MCPs. All timings for the pulsed valve, discharge, lasers, and detector were controlled by a series of commercial pulse generators (Berkeley Nucleonics Corp. and Stanford Research Systems) with 10 Hz repetition rates. Typically, data were accumulated over 10 000 laser shots to produce each final 2D raw image.

III. RESULTS AND DISCUSSION

Representative velocity map images of $S(^3P_J)$ atoms from SH predissociation are shown in Fig. 3. The results derived from analysis of the intensities and angular dependence of such images are presented in this section as branching ratios for the $J=0$, 1, and 2 spin-orbit levels and as m-state populations and recoil anisotropy parameters. The data provide clear evidence for nonadiabatic dissociation pathways following coupling from the $A\ ^2\Sigma^+$ state onto one or more repulsive PE curves and are compared with the expectations of adiabatic and diabatic (sudden) models for the dissociation dynamics.

A. Branching into $S(^3P_J)$ spin-orbit levels

Integration of the intensities of images recorded with the dissociation laser tuned to the $P_1(1.5)$ transition of a selected

TABLE I. A comparison of the spin-orbit branching ratios for the $S(^3P_J)$ atoms formed by photodissociation of SH at 232 and 226 nm obtained in this study and by Zhou *et al.* (Ref. 25). The uncertainties in parentheses are one standard deviation derived from repeat measurements.

Wavelength (nm)		$S(^3P_0)$	$S(^3P_1)$	$S(^3P_2)$
232	Current work	0.44 (0.02)	0.35 (0.03)	0.21 (0.02)
	Zhou *et al.*	0.50 (0.03)	0.36 (0.01)	0.14 (0.02)
226	Current work	0.52 (0.02)	0.30 (0.03)	0.18 (0.02)
	Zhou *et al.*	0.50 (0.08)	0.36 (0.05)	0.14 (0.07)

SH or SD $A\ ^2\Sigma^+$-$X\ ^2\Pi$ vibrational band and the detection laser tuned to the frequencies of the (2+1) REMPI transitions for the $S(^3P_J)$ levels with $J=0$, 1, and 2 allows the branching between spin-orbit states of this photofragment to be deduced. The image intensity ratios depend not only on the relative populations of the three spin-orbit levels, however, but are also influenced by the transition strengths for the two-photon excitations used for the state-specific product detection. Table I shows measurements of the branching into $S(^3P_J)$ levels following 232 and 226 nm excitations of SH and comparison with values derived by Zhou *et al.*[25] using the HR-PTS technique, from which the REMPI transition strengths are deduced to be approximately equal. The multiphoton ionization detection scheme used in the current work is resonance enhanced at the two-photon level by the $S(3p^3 4p\ ^3P_J)$ levels and has been employed previously by Hsu *et al.*[40] and Brouard *et al.*[41] The former study demonstrated that the line strengths for the individual transitions are very similar, in agreement with our measurements. The integrated image intensities can depend on the direction of polarization of the linearly polarized probe laser, but this effect, which depends on the electronic alignment of the S atoms, is minimized for the *VH* geometry. Thus *VH* image intensities were used to derive spin-orbit branching ratios without further correction.

To avoid bias in the branching ratio measurements, efforts were made to keep the experimental conditions constant for each series of measurements. Particular care was taken to ensure that the pressures of H_2S were kept constant (both the backing pressure before the valve and the pressure within the chamber) and the laser overlap was maintained, although some minor drift in laser alignment is expected on changing the frequency of the probe laser.

Table II shows the $S(^3P_J)$ spin-orbit branching ratios derived from the experimental data for predissociation of $SH(A\ ^2\Sigma^+, v=0, 1, \text{and } 2)$ and $SD(A\ ^2\Sigma^+, v=0, 1, \text{and } 2)$, and the values are plotted as a function of total kinetic energy release (TKER) of the photofragments (i.e., excess energy above the dissociation limit) in Fig. 4. The ratios are obtained from averages of three to five sets of images and the uncertainties account for the reproducibility of the measurements and include systematic errors that derive from the assumption of equal line strengths for the REMPI transitions used. From the data in the table and figure, it is evident that the dominant products are $S(^3P_2)$ atoms, with minor branching into the $S(^3P_1)$ and $S(^3P_0)$ spin-orbit levels. For $SH(A,v=0-2)$, the branching to $S(^3P_0)$ is generally observed to be greater than to $S(^3P_1)$ atoms, but for $SD(A,v=0-2)$, any preference for $S(^3P_0)$ over $S(^3P_1)$ is not so clear-cut. There is an apparent increase in the branching to $S(^3P_0)$ at the expense of $S(^3P_2)$ for $SH(A,v=2)$ predissociation.

TABLE II. Spin-orbit branching ratios for the $S(^3P_J)$ atoms formed by predissociation of the $v=0-2$ levels of $SH(A\ ^2\Sigma^+)$ and $SD(A\ ^2\Sigma^+)$. The uncertainties are one standard deviation derived from repeat measurements combined with errors resulting from the assumed direct conversion from intensity ratio to branching ratio.

	$S(^3P_0)$	$S(^3P_1)$	$S(^3P_2)$
$SH(A,v=0)$	$0.13^{+0.10}_{-0.09}$	$0.07^{+0.07}_{-0.03}$	$0.80^{+0.09}_{-0.10}$
$SH(A,v=1)$	$0.18^{+0.07}_{-0.04}$	$0.06^{+0.06}_{-0.02}$	$0.76^{+0.06}_{-0.08}$
$SH(A,v=2)$	$0.34^{+0.07}_{-0.05}$	$0.04^{+0.06}_{-0.02}$	$0.62^{+0.04}_{-0.08}$
$SD(A,v=0)$	$0.03^{+0.08}_{-0.03}$	$0.01^{+0.06}_{-0.01}$	$0.96^{+0.04}_{-0.08}$
$SD(A,v=1)$	$0.12^{+0.08}_{-0.02}$	$0.08^{+0.07}_{-0.03}$	$0.80^{+0.07}_{-0.09}$
$SD(A,v=2)$	$0.08^{+0.06}_{-0.02}$	$0.07^{+0.06}_{-0.02}$	$0.85^{+0.02}_{-0.07}$

The correlation diagram for SH (and SD) shown in Fig. 5 can be used to account for the greater propensity for $S(^3P_2)$ production. Some of the details concerning the construction of this diagram are addressed is Sec. III B 2 and the Appendix. The model proposed by Wheeler *et al.*[21] attributes the predissociation of the $v=0-2$ vibrational levels of the SH or SD $A\ ^2\Sigma^+$ state to a spin-orbit mediated interaction almost exclusively with the $\Omega=\frac{1}{2}$ component of the $1\ ^4\Sigma^-$ state; only for higher vibrational levels of SH(*A*) and SD(*A*) does coupling to the $1\ ^2\Sigma^-$ and $1\ ^4\Pi$ states become competitive with or dominant over the coupling to the $1\ ^4\Sigma^-$ state. The adiabatic correlation of the $1\ ^4\Sigma^-_{1/2}$ state is to $H(^2S_{1/2})+S(^3P_2)$ fragments, and our results thus suggest that the majority of dissociative flux follows this adiabatic pathway or crosses to the $^2\Pi_{1/2}$ component of the ground electronic state, which also dissociates to this limit (see Sec. III B 2). Branching to the other $S(^3P_J)$ spin-orbit states might arise from couplings from the $A\ ^2\Sigma^+$ state directly to the $1\ ^2\Sigma^-$ state or the $\Omega=\frac{1}{2}$

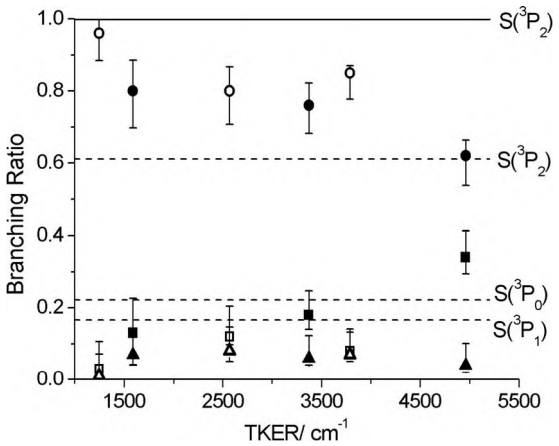

FIG. 4. Spin-orbit branching ratios for $S(^3P_J)$ plotted against TKER. Experimental fractions of $J=2$ (circles), $J=1$ (triangles), and $J=0$ (squares) for SH (filled symbols) and SD (open symbols) are compared to the predictions at the adiabatic (solid line) and the diabatic (dashed lines) limits.

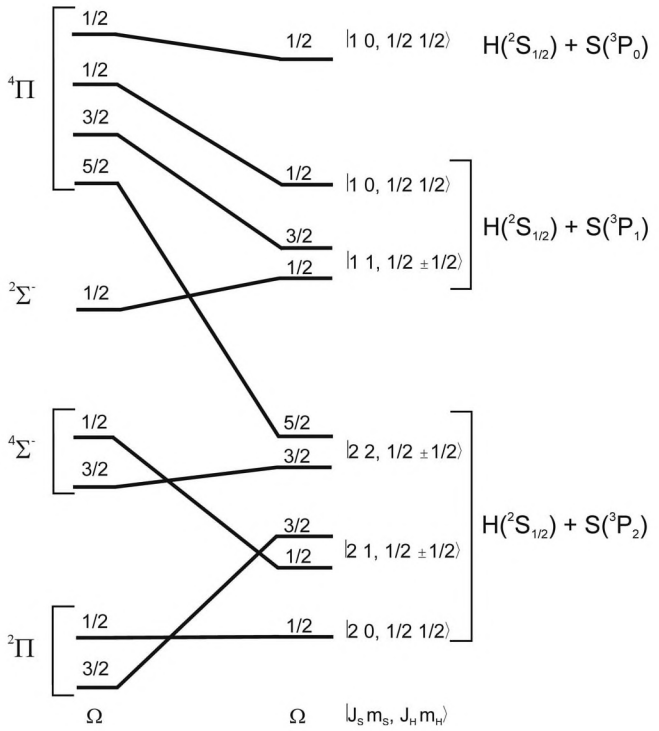

FIG. 5. Correlation diagram for SH(D) showing the correlation of the ground $X\ ^2\Pi$ and the excited $^4\Sigma^-$, $^4\Pi$, and $^2\Sigma^-$ states of SH with the $H(^2S)+S(^3P)$ asymptote. The $A\ ^2\Sigma^+$ state (not shown) is bound and correlates to $S(^1D)+H(^2S)$ fragments. The total angular momentum projection quantum number Ω and the atomic projection quantum numbers m_S and m_H have been specified. Spin-orbit mediated interactions between states follow the $\Delta\Omega=0$ selection rule, and correlations are thus determined by consideration of the energy ordering of states of the same Ω.

components of the $1\ ^4\Pi$ state, which correlate adiabatically with the other spin-orbit components. The evidence from previous FGR calculations of predissociation rates[21,23] suggests, however, that this is not the case, with the possible exception of the SH($A,v=2$) radicals. It is more likely that the branching to the $S(^3P_1)$ and $S(^3P_0)$ photoproducts occurs at larger internuclear separations, following bond extension on the repulsive $1\ ^4\Sigma^-$ state. The diabatic $^4\Sigma^-$ and $^4\Pi$ states are spin-orbit coupled,[24] but $^4\Sigma^-$-$^2\Sigma^-$ interaction is forbidden via first-order spin-orbit coupling.[42] There are thus likely to be regions along the S–H bond extension coordinate where nonadiabatic (derivative) couplings exist between the adiabatic $\Omega=\frac{1}{2}$ components of the $^4\Sigma^-$ and $^4\Pi$ states that mix dissociative flux onto the higher lying of these two PE curves. Further mixing to the adiabatic $1\ ^2\Sigma^-$ state is then possible. These deductions are broadly consistent with the arguments presented by Zhou *et al.*[25] to account for the branching between $S(^3P_J)$ fine-structure states following direct photoexcitation to the repulsive $1\ ^2\Sigma^-$ state. The extent to which $S(^3P_2)$ population is favored is, however, greater for predissociation of the low-lying vibrational levels of the $A\ ^2\Sigma^+$ state than for the direct excitation of the $1\ ^2\Sigma^-$ state, most likely reflecting the different asymptotic adiabatic correlations, as shown in Fig. 5.

The increase in the branching to $S(^3P_0)$ products for SH($A,v=2$) predissociation is consistent with the onset of coupling from the $A\ ^2\Sigma^+$ state to the $1\ ^4\Pi$ state either directly or via initial $A\ ^2\Sigma^+$-$1\ ^2\Sigma^-$ coupling. As Fig. 5 shows, one $\Omega=\frac{1}{2}$ component of the $1\ ^4\Pi$ state correlates adiabatically to the $S(^3P_0)$ state. Wheeler *et al.*[21] estimated direct $A\ ^2\Sigma^+$-$1\ ^4\Pi$ coupling to be negligible, but coupling to the $1\ ^2\Sigma^-$ state amounts to $\leq 10\%$ of the main channel to the $1\ ^4\Sigma^-$ state at this vibrational level. More recent calculations by Brites *et al.*[23] suggested that direct coupling to the $1\ ^2\Sigma^-$ state contributes about 25% of the total predissociation rate for SH($A,v=2$) [but it remains a negligible pathway for SH($A,v=0,1$) and SD(A, $v=0$, 1, and 2), in accord with the deductions of Wheeler *et al.*]. As Fig. 1 shows, the crossing of the $1\ ^4\Pi$ state with the outer wall of the $A\ ^2\Sigma^+$ state lies too high in energy to influence the predissociation dynamics of these low vibrational levels.

The observation of S atoms populating spin-orbit levels other than expected from adiabatic correlation arguments is clear evidence for nonadiabatic dynamics between the three sets of repulsive potentials correlating to the $H(^2S)+S(^3P)$ limit. Comparisons can be made with the expectations of a "sudden" or diabatic model in which the electronic wave functions of the molecular states are projected onto a basis of atomic states for this dissociation limit. The results of such calculations, the procedures for which are explained in detail elsewhere,[27] are shown in Table III and included in Fig. 4. While the fully diabatic model for the $1\ ^4\Sigma^-_{1/2}$ state dissociation agrees qualitatively with the experimental observations, for example, in favoring the $J=2$ spin-orbit level, with near equal propensities for the $J=1$ and 0 levels, the experiments show a greater branching into $S(^3P_2)$ products. The dynamics following coupling from the $A\ ^2\Sigma^+$ state to the $1\ ^4\Sigma^-$ state can thus not be viewed as occurring either in the purely adiabatic or diabatic limits, and an intermediate picture must be invoked.

TABLE III. $S(^3P_J)$ spin-orbit branching ratios $P(J)$ for predissociation of SH(A) via the $1\ ^4\Sigma^-$ and $1\ ^2\Sigma^-$ states calculated in the sudden or diabatic limit and the associated population distribution p_m over available m states, where p_m is the total population of the $+m$ and $-m$ states when m is nonzero.

	$1\ ^4\Sigma^-_{1/2}$				$1\ ^2\Sigma^-_{1/2}$			
		p_m				p_m		
J	$P(J)$	$m=0$	$m=\pm1$	$m=\pm2$	$P(J)$	$m=0$	$m=\pm1$	$m=\pm2$
0	0.222	1.000	⋯	⋯	0.111	1.000	⋯	⋯
1	0.167	0.000	1.000	⋯	0.333	0.000	1.000	⋯
2	0.611	0.727	0.273	0.000	0.555	0.400	0.600	0.000

B. Recoil velocity anisotropy and angular momentum polarization

The velocity map images of the photofragments show angular dependence to their intensities because of a combination of the effects of spatial anisotropy in both the recoil velocities and electronic angular momenta of the $S(^3P_J)$ atoms. The experiments are sensitive to the angular momentum polarization because the 2+1 REMPI detection scheme employs linearly polarized light. The lifetimes of the vibrational levels of the $A\ ^2\Sigma^+$ state studied here range from a few picoseconds to many nanoseconds and are thus comparable to or much longer than the rotational period of the molecules. Nevertheless, the predissociation can result in an anisotropic distribution of photofragment recoil velocities (p_v).[32,33] Within the axial recoil approximation, the recoil velocity vector for dissociation of a diatomic molecule lies parallel to the internuclear bond axis, and a preferred distribution of the planes of rotation of the ensemble of excited state molecules in space, prepared by absorption of polarized light, can thus maintain an overall anisotropy of the recoil velocity vectors of the atomic photofragments.

The state-specific detection of $S(^3P_J)$ atoms with $J=0$, 1, and 2 means that each velocity map image contains information on only a single fragmentation channel. Analysis of the variation of intensity with angle for the outermost few pixels of the 2D velocity map images is thus equivalent to analysis of a slice through the three dimensional (3D) reconstruction of the Newton sphere of recoil velocities of the nearly monoenergetic photofragments and might be expected to show an intensity variation of the form described by[43]

$$p_v(\theta) = \frac{1}{4\pi}[1 + \beta_v P_2(\cos\theta)]. \tag{1}$$

Here, $p_v(\theta)$ is the product angular distribution with respect to θ, the angle between the linear polarization of the photolysis laser (ε) and the direction of product recoil (v) in the laboratory frame. $P_2(x)=\frac{1}{2}(3x^2-1)$ denotes a second Legendre polynomial, and the anisotropy parameter β_v takes limiting values of $+2$ for a parallel transition and -1 for a perpendicular transition followed by prompt dissociation. In practice, this intensity distribution is further modulated by the sensitivity of the probe laser polarization to the angular momentum alignment of the photofragments [the detection efficiency $I_{\mathrm{det}}(\theta)$], resulting in a general expression for the intensity variation with image angle:

$$I(\theta) \propto p_v(\theta) I_{\mathrm{det}}(\theta) = \frac{1}{4\pi}[1 + \beta_2 P_2(\cos\theta) + \beta_4 P_4(\cos\theta) + \beta_6 P_6(\cos\theta)]. \tag{2}$$

The values of the parameters β_2, β_4, and β_6 depend on the recoil anisotropy, the angular momentum polarization of the products, the polarizations of the photolysis and probe lasers, and the plane of the imaging detector. In the following analysis of image angular variation to extract quantitative information on photofragment velocity anisotropy and angular momentum alignment, we follow the procedures employed by Coroiu *et al.*,[44] which were based on the work of Mo and Suzuki.[45,46] The resultant velocity anisotropy parameters are compared with expectations for a predissociative system using the method of Kim *et al.*[32] Angular momentum alignment is presented in terms of populations of magnetic sublevels of the $S(^3P_J)$ atoms with $J=1$ or 2, which are indicative of the degree of nonadiabatic dissociation dynamics. The general analysis procedures are first reviewed and then the β_v parameter values and $S(^3P_J)$ spin-orbit resolved m-state populations are discussed separately.

The outermost rings (two to three pixels wide) of the velocity map images were fitted to the angular function given in Eq. (2). In all cases, incorporation of a $P_6(\cos\theta)$ function made no discernible difference to the quality of the fits, and the expansion in Eq. (2) was thus truncated at fourth-order terms, giving two fit parameters, β_2 and β_4, for each image. The detection efficiency of the photofragments with aligned electronic angular momenta can be expressed as

$$I_{\mathrm{det}}(\theta) = \sum_k \rho^{(k)}_{0,\mathrm{PF}} P_k(J_f, J_i), \tag{3}$$

where $P_k(J_f,J_i)$ are line-strength factors for the two-photon transition between levels with angular momentum quantum numbers J_i (initial state) and J_f (final state). The $\rho^{(k)}_{0,\mathrm{PF}}$ are the components with $q=0$ of rank-k multipole moments of the density matrix describing the populations and coherences of the magnetic sublevels with angular momentum quantum number J_i and projection quantum numbers m. The projections are defined with respect to the probe laser linear polarization vector, and the subscript PF thus denotes the probe frame. The index k takes values of 0, 2, and 4 for a probe transition induced by linearly polarized light and resonance enhanced at the two-photon level. When $J_i \neq J_f$, Mo and Suzuki[46] demonstrated that the ratios of the line-strength factors with $k=2$ and 4 to the $k=0$ factor simplify to the convenient form (expressed here for linearly polarized light)

$$\tilde{P}_k(J_f,J_i) = P_k(J_f,J_i)/P_0(J_f,J_i) = 5\sqrt{2k+1}\sqrt{2J_i+1}(-1)^{J_i+J_f}\begin{pmatrix} 2 & 2 & k \\ 0 & 0 & 0 \end{pmatrix} \times \begin{Bmatrix} J_i & J_i & k \\ 2 & 2 & J_f \end{Bmatrix}. \tag{4}$$

Evaluation of the 3-j and 6-j symbols in this expression for the REMPI transitions employed gives $\tilde{P}_2(1,2)=-\sqrt{5/14}$ and $\tilde{P}_4(1,2)=-2\sqrt{2/7}$ for the $S(3p^3 4p)\,^3P_1 \leftarrow\!\!\leftarrow {}^3P_2$ two-photon excitation and $\tilde{P}_2(2,1)=1/\sqrt{2}$ and $\tilde{P}_4(2,1)=0$ for the $S(3p^3 4p)\,^3P_2 \leftarrow\!\!\leftarrow {}^3P_1$ transition. For transitions from the $^3P_0$ level, the $k=2$ and 4 line-strength factors are, by definition, zero.

Two geometries of laser polarizations were employed for the measurements; in both cases the photolysis laser was polarized vertically in the laboratory (denoted V, and parallel to the detector face), but the probe laser was polarized either vertically (specified hereafter as VV geometry) or horizontally (VH geometry). If we take a laboratory frame of reference defined by Cartesian axes with Z parallel to the vertical polarization of the photolysis laser, X the axis of propagation of the two laser beams, and Y the axis along the TOF tube

toward the detector (see Fig. 2), the probe laser polarization lies either along the Z or Y axes (V or H, respectively) and the detector lies parallel to the XZ plane. Rotation from the frame defined by the photofragment recoil velocity vector [the recoil frame (RF)] to the probe laser frame transforms the multipole moments of the angular momentum in accord with

$$\rho_{q,\mathrm{PF}}^{(k)} = \sum_{q'=-k}^{k} \rho_{q',\mathrm{RF}}^{(k)} D_{q'q}^{(k)}(\Phi,\Theta,\chi), \tag{5}$$

where $D_{q'q}^{(k)}(\Phi,\Theta,\chi)$ is a Wigner rotation matrix, and the Euler angles (Φ,Θ,χ) link the two frames of reference. In the case of the VV polarization geometry, we identify $(\Theta,\Phi)=(\theta,\phi)$, the polar and azimuthal angles of the recoil velocity vector in the PF (which is equivalent to the frame defined by the photodissociation laser polarization), and θ also corresponds to the polar angle in the image plane. For the VH geometry, we make the identification that $\Phi=\pi/2$, $\Theta=\pi/2$, and $\chi=\theta$ (considering that the outermost ring in the image arises from recoil velocities in the XZ plane). The analysis is further simplified if we make the assumptions that the angular momentum polarization is cylindrically symmetric about the recoil velocity vector and independent of direction. A consequence is that only $q'=0$ components of $\rho_{q',\mathrm{RF}}^{(k)}$ are nonzero, and we neglect the effects of coherences between m states but can derive information on fractional populations of these m states (f_m) in the RF from

$$\rho_{0,\mathrm{RF}}^{(k)} = \sum_{m=-J_i}^{J_i} (-1)^{J_i-m}\sqrt{2k+1}\begin{pmatrix} J_i & k & J_i \\ -m & 0 & m \end{pmatrix} f_m. \tag{6}$$

With the above approximations, Eq. (5) reduces to

$$\rho_{0,\mathrm{PF}}^{(k)} = \rho_{0,\mathrm{RF}}^{(k)} P_k(\cos\,\theta) \tag{7}$$

for the VV polarization geometry and

$$\rho_{0,\mathrm{PF}}^{(k)} = \rho_{0,\mathrm{RF}}^{(k)} P_k(\cos\,\pi/2) \tag{8}$$

for the VH geometry. Substitution of Eqs. (4) and (7) or Eq. (8) into Eq. (3) and re-expression of the result as a single expansion in Legendre polynomials allows us to evaluate Eq. (2) as

$$\begin{aligned} I(\theta) &\propto [1+\beta_v P_2(\cos\,\theta)]\sum_k \rho_{0,\mathrm{RF}}^{(k)} \tilde{P}_k(J_f,J_i) P_k(g(\theta)) \\ &= \sum_{l=0}^{6} \beta_l P_l(\cos\,\theta), \end{aligned} \tag{9}$$

where $g(\theta)$ denotes $\cos\,\theta$ for the VV geometry and $\cos(\pi/2)$ for the VH geometry. The expansion coefficients used in Eq. (2) are obtained as

$$\begin{bmatrix} \beta_0 \\ \beta_2 \\ \beta_4 \\ \beta_6 \end{bmatrix} = \begin{bmatrix} 1 & \frac{1}{5}\beta_v & 0 \\ \beta_v & 1+\frac{2}{7}\beta_v & \frac{2}{7}\beta_v \\ 0 & \frac{18}{35}\beta_v & 1+\frac{20}{77}\beta_v \\ 0 & 0 & \frac{5}{11}\beta_v \end{bmatrix} \begin{bmatrix} \tilde{P}_0(J_f,J_i)\rho_{0,\mathrm{RF}}^{(0)} \\ \tilde{P}_2(J_f,J_i)\rho_{0,\mathrm{RF}}^{(2)} \\ \tilde{P}_4(J_f,J_i)\rho_{0,\mathrm{RF}}^{(4)} \end{bmatrix} \tag{10}$$

for the VV geometry and

$$\begin{bmatrix} \beta_0 \\ \beta_2 \\ \beta_4 \\ \beta_6 \end{bmatrix} = \begin{bmatrix} 1 & -\frac{1}{2} & \frac{3}{8} \\ \beta_v & -\frac{1}{2}\beta_v & \frac{3}{8}\beta_v \\ 0 & 0 & 0 \\ 0 & 0 & 0 \end{bmatrix} \begin{bmatrix} \tilde{P}_0(J_f,J_i)\rho_{0,\mathrm{RF}}^{(0)} \\ \tilde{P}_2(J_f,J_i)\rho_{0,\mathrm{RF}}^{(2)} \\ \tilde{P}_4(J_f,J_i)\rho_{0,\mathrm{RF}}^{(4)} \end{bmatrix} \tag{11}$$

for the VH geometry.

The image analysis thus involves fitting of the angular dependence to Eq. (2) to obtain experimental values of the coefficients β_2 and β_4 with normalization to $\beta_0=1$ and neglect of the β_6 term. These β_i values can be simultaneously forward simulated for both VV and VH geometries by calculating $\rho_{0,\mathrm{RF}}^{(k)}$ values from Eq. (6) by cycling over possible combinations of populations of the m states and combining the values with β_v values in the range from -1 to $+2$. For an aligned sample, $f_m=f_{-m}$, and we thus imposed this restriction on the simulations, together with the requirement that the populations of all m states sum to unity. It proved useful to define $p_m=f_m$ for $m=0$ and $p_m=f_{-m}+f_m$ for $m\neq 0$. The forward simulation procedure was carried out using a simple computer program with a step size of 0.01 for both p_m and β_v to find optimum values for these parameters to reproduce the experimental β_2 and β_4 data for both VV and VH geometries, with use of the line-strength factors appropriate for each $S(^3P_J)$ state studied. Thus, recoil velocity anisotropy parameters and angular momentum alignment information were deconvoluted from the experimental angular distributions. Such an analysis is not, however, necessary for $S(^3P_0)$ atoms because the $J=0$ level cannot show any angular momentum alignment effects, and its detection probability is independent of probe laser polarization.

The analysis method requires that $J_i\neq J_f$ in the two-photon absorption step in the REMPI scheme. In the case of $S(^3P_J)$ detection via the $3p^34p\ (^3P)\leftarrow\leftarrow 3p^3(^3P)$ excitation scheme, however, the components of the transition with $J_f=0$, 1, and 2 are only partially resolved within the linewidth of the laser. For $S(^3P_2)$ detection, the $^3P_2\leftarrow\leftarrow{}^3P_2$ component is stronger than for excitation to the $^3P_1$ and $^3P_0$ levels,[40] and several images were thus accumulated using this $\Delta J=0$ transition. To test the robustness of our methods, measurements of angular distributions and analysis to derive β_v and m-state populations were therefore made at probe laser wavelengths on the sides of the broad REMPI feature corresponding to the $^3P_1\leftarrow\leftarrow{}^3P_2$ and $^3P_2\leftarrow\leftarrow{}^3P_2$ transitions. At the chosen wavelengths, we estimate that there are $\sim$15% and $<$5% contributions, respectively, from the overlapping transitions. The values of β_v obtained showed no dependence on the choice of REMPI wavelength within this two-photon excitation feature, and m-state populations required only a small correction (by factors of 1.3, 0.9, and 1.0 for $m=0$, ± 1, and ± 2) to make the values derived from data

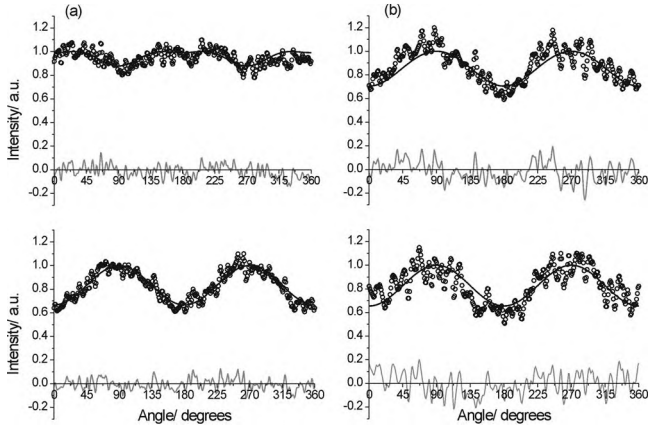

FIG. 6. Experimental angular distributions (open circles) from which anisotropy parameters and alignment information are obtained: (a) S($^3P_2$) images and (b) S($^3P_1$) images for the SD(v=1), Q_1(1.5) line. The upper graphs correspond to *VV* geometry images and the lower graphs to *VH* geometry. The solid lines are simulations of the angular dependence obtained using Eq. (2) and the values of β and *m*-state populations from the data analysis procedure described in the text. The gray lines indicate the differences between experimental data and the simulations.

obtained in the $^3P_2 \leftarrow\leftarrow {}^3P_2$ wing of the feature match those from the $^3P_1 \leftarrow\leftarrow {}^3P_2$ wing. A similar investigation of the S($^3P_1$) REMPI detection scheme, for which the $^3P_2$ and $^3P_1$ upper state components are also incompletely resolved, showed that within experimental error, no correction was required for either β_v or *m*-state populations derived from images obtained at excitation wavelengths across the spectral feature.

In most cases of fitting to the angular dependence of the outer parts of velocity map images, the fits are good, and Fig. 6 compares the experimental data with simulations obtained using Eq. (2) and β_2 and β_4 values derived from the analysis described above. The simulations capture the main features of the angular distributions, such as the depth of modulation. The largest discrepancies tend to be for data obtained via *R* branch transitions, most notably for SH(v=1). A further test of the success of the fits, which serves to examine the consequences of approximations made in the analysis of the data to derive *m*-state populations, is to compare the outcomes for the *VH* geometry with the expectations from Eq. (11) that $\beta_2/\beta_0=\beta_v$ and $\beta_4=0$. In almost all cases, these expectations are met within the uncertainties in the derived parameters: values of β_2/β_0 from the fits differ from the β_v values resulting from the data analysis by less than 0.05 in the majority of cases, with the main exceptions being *R* branch excitations to SH and SD(A,v=1) and to SH(A,v=2). The magnitudes of $\beta_4(VH)$ parameters are generally less than 0.1, with the exception of S($^3P_2$) and S($^3P_1$) atoms resulting from *R* branch excitation to SH(A,v=1) and *Q* and *R* branch transitions to SH(A,v=2). These highlighted discrepancies may arise from signal-to-noise ratios in the experimental images or may imply some degree of breakdown in one of the assumptions made in the analysis, such as the neglect of coherences between *m* states. Comparisons of relative intensities in *VV* and *VH* images could, in principle, provide additional information on the effects of coherences but were not possible in the current study because *VV* and *VH* images were accumulated separately rather than with shot-to-shot variation of the probe laser polarization.

Further errors in retrieved anisotropy parameter and *m*-state population values might arise because of our analysis of the angular variation of the outermost two to three pixels of the images. This method was preferred to Abel inversion of the data to obtain an *XZ* plane slice through the 3D Newton sphere. For the slow-moving S atom photofragments, image radii varied from 9 to 25 pixels depending on the choice of excited vibrational level of the SH or SD($A\ ^2\Sigma^+$) radicals, and the 2–3 pixel range analyzed corresponded to the resolution of the imaging detection. One consequence of the finite slice width is that some S atom recoil velocity vectors that are out of the *XZ* plane will be included in our analysis, but we estimate that these lie within 30° of the plane and thus will not have significant consequences for derived β_v parameters and *m*-state populations. Indeed, prior tests showed that the obtained values of β_v were not significantly affected by the choice of pixel range made here.

The β_v and p_m values derived from the experiments require rather different types of interpretation and are thus discussed separately in the following sections.

1. Anisotropy parameters for SH(*A*) and SD(*A*) predissociation

The treatment of the anisotropy parameters resulting from predissociation of states with lifetimes comparable to or longer than their rotational periods has been the subject of recent studies by Kim *et al.*[32] and Kuznetsov and Vasyutinskii.[33] Here, we compare the outcomes of our experimental measurements of β_v parameters for predissociation of different vibrational levels of SH(A) and SD(A) with the predictions of the model proposed by Kim *et al.*[32] using the computer program BETAOFNU.[34] This model accounts for the polarization of the internuclear axis caused by absorption of linearly polarized light, the effects of the rotational motion of the excited state, and interference effects in the spatial distribution of photofragments caused by overlapping *P*, *Q*, and *R* branch absorption features. The model does not explicitly deal with the state-specific detection of atomic fragments in individual spin-orbit states nor does it take into account possible depolarization of the spatial distribution of the internuclear axis caused by coupling of the rotational and electronic angular momenta of the SH or SD to the nuclear spin of the H or D atom (hyperfine depolarization effects). The consequences of hyperfine depolarization on β_v values are discussed further below.

Figure 7 shows experimentally determined β_v values for SH(v=2) obtained by detection of S($^3P_2$) and S($^3P_0$) in the *VH* geometry. Equation (11) demonstrates that no alignment effects are expected in this geometry and thus $\beta_2=\beta_v$; experimental fits to Eq. (2) largely confirm this, as was noted at the end of the previous section. The short lifetime of SH(A,v=2) means that spectroscopic lines are sufficiently broadened that a number of β_v values could be obtained experimentally for photoexcitation across the wavenumber range from 34 190 to 34 260 cm^{-1} to investigate the frequency dependence of β_v. The data in Fig. 7 show an oscil-

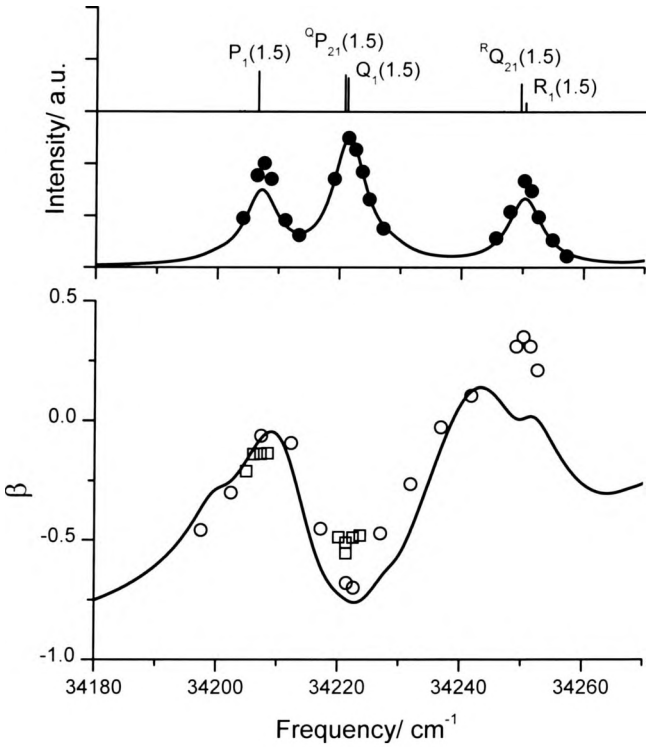

FIG. 7. A comparison between calculations and experiment for predissociation via SH($A,v=2$). The top panel shows a plot of the calculated (solid line) and experimental (points) spectrum, above which is a stick spectrum indicating the assignments of the spectral lines (with the stick heights indicative of the relative intensities). The bottom panel compares calculated (solid line) and experimental values of β_v for S($^3P_2$) (circles) and S($^3P_0$) (squares) atom products.

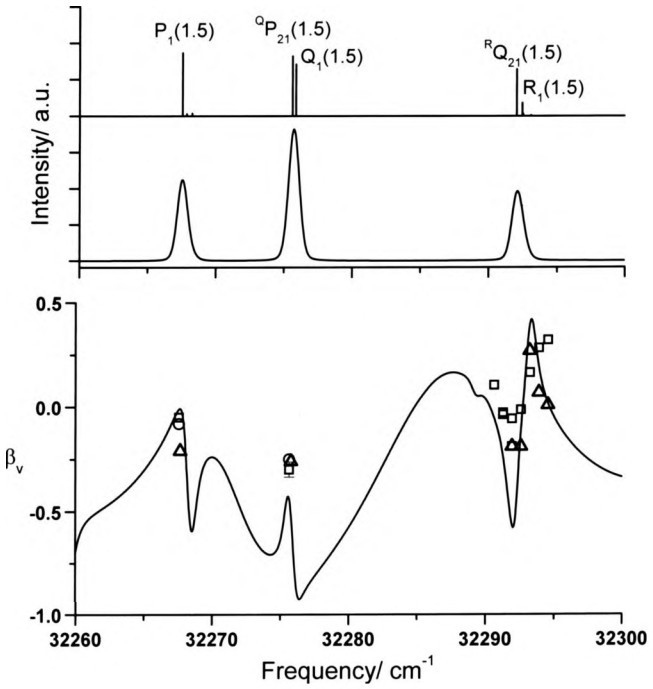

FIG. 8. A comparison between calculations and experiment for predissociation via SD($A,v=1$). The top panel shows a plot of the calculated spectrum, above which is a stick spectrum (as in Fig. 7). The bottom panel compares calculated (solid line) and experimental values of β_v for S($^3P_2$) (circles), S($^3P_1$) (triangles), and S($^3P_2$) (squares) atom products.

lation in β_v values because of interference effects arising from the excitation of the overlapped transitions.[32] Analysis of the integrated image intensities for the different excitation wavelengths, the results of which are plotted in Fig. 7 as a coarse experimental spectrum, together with a simulated spectrum (obtained using the PGOPHER program[47]), gives a best estimate of the Lorentzian line broadening of 6.8 cm^{-1} full width at half maximum (FWHM) that corresponds to a lifetime for the SH($A,v=2$) rotational levels of ~0.8 ps. This estimate is shorter by factors of ~3–6 than lifetimes predicted by the existing theoretical models of predissociation of the $A\ ^2\Sigma^+$ state of SH.[21,23] Incorporation of this lifetime into calculations of expected β_v values enables a comparison to be made between measurements and predictions, and the results are shown in the lower panel of the figure. The theoretical model of Houston and co-workers captures well both the magnitudes and wavelength dependence of the recoil velocity anisotropy, although there are some small discrepancies in the vicinity of the $R_1(1.5)+{}^RQ_{21}(1.5)$ feature.

Similar comparisons were drawn with the β_v values obtained from measurements of predissociation following excitation of SH and SD (A, $v=0$ and 1) on the $P_1(1.5)$, $Q_1(1.5)+{}^QP_{21}(1.5)$ and $R_1(1.5)+{}^RQ_{21}(1.5)$ spectral lines, although no measurements of angular distributions were made for the S($^3P_0$) and S($^3P_1$) photofragments arising from predissociation of SD($A,v=0$) because of low signal levels. The simulations of anisotropy parameters used upper state lifetime values taken from spectroscopic studies of fluorescence lifetimes and spectral line broadening[18,20,21] and the computed frequency dependent β_v values were then convoluted with a Gaussian function with a FWHM of 0.6 cm^{-1} to mimic the effects of the laser bandwidth in the experiments. An example set of data is shown in Fig. 8 for SD($A,v=1$). The agreement between experimental and calculated values was poorer for these data than for the SH($A,v=2$) results, with the measured β_v values consistently smaller in magnitude than the expectations of the theoretical model [with the exception of the $P_1(1.5)$ line for which the calculated $\beta_v=0.0$ was as expected for an upper state with $J=\frac{1}{2}$ and $N=0$]. For SH($A,v=0$) and SD($A,v=0$), the measured anisotropy parameters all lie close to zero The lifetimes of the SH($A,v=0$) and SD($A,v=0$) levels are, respectively, 3.2 and 250 ns for low rotational levels,[18,20,21] and these lifetimes are not only considerably longer than the rotational periods but are also comparable to or longer than the characteristic time scales for coupling of the nuclear spins of the H or D atoms to the rotational and electronic spin angular momenta of the SH or SD radicals. The nuclear hyperfine splittings for SH($A,v=0$) were reported by Ubachs *et al.*,[18] and, for J values up to 5/2, range from 289.9 to 898.6 MHz. Taking a representative value of $\nu_{HF}=500$ MHz, the time scale for hyperfine coupling of J with I_H to give the resultant total angular momentum F is $\tau=2\pi/\nu_{HF}\sim12$ ns and about an order of magnitude longer for SD.[48] The nuclear spin of ^{32}S is $I_S=0$, and it thus does not play a part in the following discussion.

We consider the hyperfine coupling interactions further because they can cause depolarization of the optically prepared spatial alignment of rotational angular momentum (de-

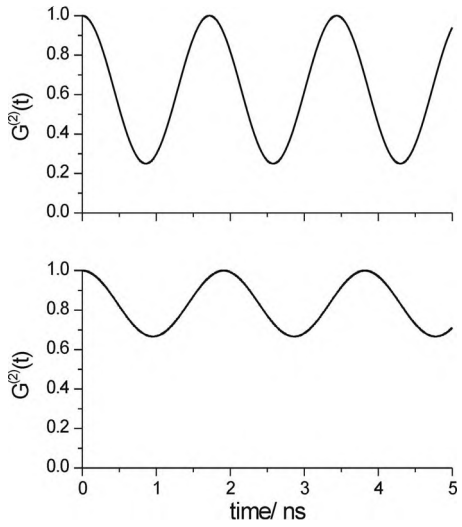

FIG. 9. Calculated $G^{(2)}(t)$ hyperfine depolarization factors for pure $Q_1(1.5)$ (top panel) and $R_1(1.5)$ (bottom panel) transitions.

noted here by a quantum number N) or internuclear axes of the SH or SD. Depolarization of N by S (the electronic spin angular momentum) is treated implicitly in the computer simulations described so far, but hyperfine depolarization is not incorporated. Values of β_v can thus degrade from the expectations from calculations using the method of Kim *et al.*[32] because of precession of the nuclear framework rotational angular momentum N about J and of J about the total angular momentum F.[49] The procedures for calculation of the time-dependent depolarization of N are well established:[50–52] a rotational angular momentum alignment parameter $A_q^{(k)}(0)$ at $t=0$ is multiplied by a time-dependent hyperfine depolarization factor $G^{(k)}(t)$ of the same rank to give a time-dependent alignment parameter:

$$A_0^{(k)}(t) = A_0^{(k)}(0)G^{(k)}(t). \tag{12}$$

To account for hyperfine depolarization of β_v, Zhang *et al.*[53] simply multiplied β values by $G^{(2)}(t)$ factors in their study of photodissociation of aligned HF molecules. To verify this approach, we computed the alignment parameters $A_q^{(2)}(N)$ for one-photon excitation of a diatomic molecule via P, Q, and R branch transitions using linearly polarized light, and, using Eq. (12), applied the hyperfine depolarization appropriate for SH calculated from[51]

$$G^{(k)}(t) = \sum_{F,F'} \cos[(E_{F'} - E_F)t/\hbar)] \times \frac{(2F'+1)(2F+1)}{(2I+1)} \begin{Bmatrix} F' & F & k \\ J & J & I \end{Bmatrix}^2 \tag{13}$$

and knowledge of splittings of hyperfine energy levels, $E_{F'} - E_F$. Figure 9 shows the time dependence of the $G^{(2)}(t)$ parameters for excitation of SH via the $Q_1(1.5)$ and $R_1(1.5)$ transitions. The resultant depolarized angular momentum alignment parameters were used to calculate the associated internuclear axis alignment parameter in the presence of hyperfine coupling. As a test of the method, these latter parameters, derived in the absence of hyperfine interactions, were compared with values of A_0, the parameter introduced by Zare[54] to describe the spatial distribution of internuclear axes of a diatomic molecule in a long-lived excited state following the absorption of linearly polarized light, and the two calculations gave identical results. In the limit of an excited state that predissociates on a time scale much longer than its rotational period, with the fragmentation occurring under conditions of axial recoil, the internuclear axis alignment parameter A_0 is equivalent to the photofragment recoil anisotropy parameter β_v and we thus deduce that the time-dependent hyperfine depolarization of β_v is correctly described by

$$\beta_v(t) = \beta_v G^{(2)}(t), \tag{14}$$

in agreement with the method of Zhang *et al.*[53] Here, the β_v values are those computed using the theory of Kim *et al.*,[32] and the time chosen in Eq. (14) corresponds to the predissociative lifetime of the SH or SD radicals in their $A\ ^2\Sigma^+$ state and a particular v and N level.

From these calculations, we conclude that hyperfine depolarization can reduce β_v values by a factor of 0.25–1 following excitation of SH to $v=0$ of the $A\ ^2\Sigma^+$ state via the $Q_1(1.5)$ line and a factor of 0.66–1 for the $R_1(1.5)$ line. The precise values depend on the predissociative lifetimes, but the respective time-averaged reduction factors are 0.68 and 0.83. We do not make a more quantitative comparison with the experimental data, however, because of the blended nature of the spectroscopic absorption lines. For higher vibrational levels of the $A\ ^2\Sigma^+$ state with lifetimes on the picosecond time scale, little or no hyperfine depolarization of β_v is expected.

2. Populations of m levels for S($^3P_1$) and S($^3P_2$) photoproducts

The angular dependences of the velocity map images for S($^3P_1$) and S($^3P_2$) photofragments show characteristic signatures of electronic angular momentum polarization in the S atoms which can be quantified in terms of unequal populations, p_m, of m sublevels. The outcomes of the data analysis procedure described above are presented in Figs. 10 and 11 and Table IV; we do not distinguish $\pm m$ level populations because the experiments are sensitive only to even rank alignment moments. The data presented in Table IV are averages of the populations of the m sublevels for the S($^3P_2$) and S($^3P_1$) atoms following excitation of SH or SD to each of the $v=0$, 1, and 2 levels of the $A\ ^2\Sigma^+$ state via $P(1.5)$, $Q(1.5)$, and $R(1.5)$ transitions. As is evident from the standard deviations of the populations presented in Table IV and as will be discussed further below, these m sublevel populations are insensitive to the use of SH or SD in the experiments, the vibrational level of the $A\ ^2\Sigma^+$ state from which predissociation occurs, or the rotational level that is excited.

There are two further clear outcomes of the measurements. The first is that the electronic angular momentum of the S($^3P_1$) atoms is polarized, with the $m=\pm 1$ levels possessing nearly four times the population of the $m=0$ level. The second is that the S($^3P_2$) atoms are also strongly polarized, with the $m=\pm 2$ levels exhibiting very little population but the $m=\pm 1$ and 0 levels both significantly and nearly

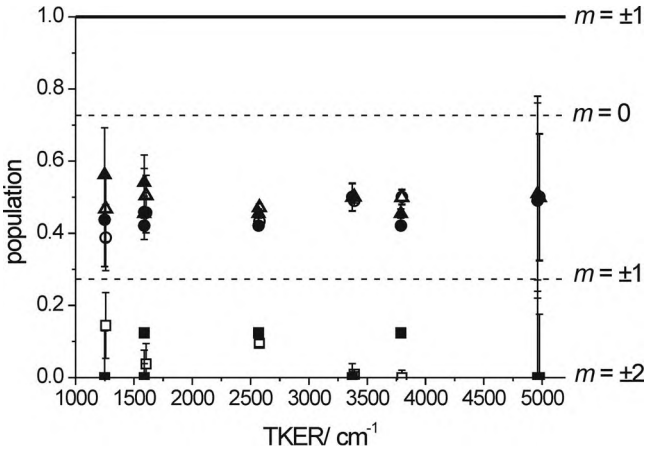

FIG. 10. m-state populations for $S(^3P_2)$ atoms as a function of TKER of the S and H atom photodissociation products. The experimentally determined populations of $m=0$ (circles), $m=\pm1$ (triangles), and $m=\pm2$ (squares) are compared to the predictions of the adiabatic (solid line) and diabatic (dashed lines) calculations for predissociation via the $1\ ^4\Sigma^-$ potential (see also Table III). Open and filled symbols are data obtained, respectively, via the $Q_1(1.5)+{}^QP_{21}(1.5)$ and $P_1(1.5)$ transitions. The errors represent the quality of the fits and are $\frac{1}{2}$ of the root mean square differences between the experimental β_2 and β_4 values obtained from fits to VV and VH images and the calculated best fit values. The larger error bars for the data points close to 5000 cm^{-1} are a consequence of poorer fits to the angular dependence of the source images.

equally populated. We note that these results derive from an analysis that neglects coherence effects among the m levels and that the angular momentum polarization is not subject to hyperfine depolarization because $I_S=0$.

Figures 10 and 11 show plots of m-state populations of the $S(^3P_2)$ and $S(^3P_1)$ atom products, respectively, for the $P_1(1.5)$ and $Q_1(1.5)+{}^QP_{21}(1.5)$ lines plotted against TKER of the atomic products. The consistency of the outcomes of the m-state populations regardless of the isotopolog, vibrational, or rotational state is clearly evident in these plots. For comparison, the predicted m-state populations for dissociation from the $^4\Sigma^-_{1/2}$ state within the adiabatic and diabatic

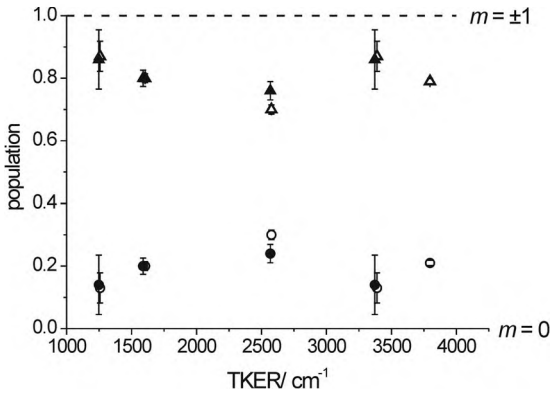

FIG. 11. m-state populations for $S(^3P_1)$ atoms as a function of TKER. The experimentally determined populations of $m=0$ (circles) and $m=\pm1$ (triangles) are compared to the predictions of diabatic (dashed line) calculations for predissociation via the $1\ ^4\Sigma^-$ potential (see Table III). Open and filled symbols are data obtained, respectively, via the $Q_1(1.5)+{}^QP_{21}(1.5)$ and $P_1(1.5)$ transitions. Note that the adiabatic model predicts no population of $S(^3P_1)$. The errors represent the quality of the fits and are $\frac{1}{2}$ of the root mean square differences between the experimental β_2 and β_4 values obtained from fits to VV and VH images and the calculated best fit values.

TABLE IV. Average m-state populations, p_m, for $S(^3P_2)$ and $S(^3P_1)$, where p_m is the total population of the $+m$ and $-m$ states when m is nonzero. The experimental average spin-orbit branching ratios, $P(J)$, are also listed. All p_m and $P(J)$ values are the average of all SH and SD data sets after correction for REMPI upper state, as described in the text, and the uncertainties in parentheses are one standard deviation derived from these measurements.

		p_m		
J	$P(J)$	$m=0$	$m=\pm1$	$m=\pm2$
1	0.06	0.21 (0.08)	0.79 (0.08)	⋯
2	0.80	0.45 (0.06)	0.54 (0.06)	0.01 (0.06)

models (see Sec. III A and Table III) are also plotted. For $S(^3P_2)$ atoms it is clear that neither the adiabatic or diabatic model captures the m-state populations quantitatively. For $S(^3P_1)$, which adiabatically should not be observed as photoproducts, the m-state populations approach the diabatic limit with the $m=\pm1$ levels exhibiting the majority of the population, but there is also non-negligible population of the $m=0$ level.

In the adiabatic model, a correlation diagram is constructed to determine the photodissociation product states. In the correlation diagram, the states are labeled by $\Omega=m_S+m_H$, with m_S and m_H, respectively, denoting the projections of the electronic angular momenta of the S and H atoms onto the internuclear axis. This axis corresponds to the RF if, as we expect, the axial recoil approximation applies. To derive the fragment polarization, the separate m_S and m_H quantum numbers must be assigned to the states, as was done for the $S(^1D_2)+H(^2S_{1/2})$ atomic limit in Ref. 27. For the $S(^3P_J)+H(^2S_{1/2})$ limit, we must take into account the nonzero spin-orbit coupling in the $S(^3P_J)$ atom. When Ω takes the highest possible value for a given atomic fine-structure state, $|Jm_S\rangle|J_Hm_H\rangle$, the only possibility is $m_S=J$ and $m_H=J_H$ (we adopt the convention that $\Omega>0$). For the other substates, there are two possibilities: $m_S=\Omega\pm\frac{1}{2}$. These two sublevels are degenerate asymptotically and the assignment is based on the energy ordering at long range. As before, the leading long-range term that lifts the degeneracy is the dispersion interaction. The energy ordering may be derived from the anisotropy of the polarizability of the sulfur atom, as derived in the Appendix, and the result is shown in Fig. 5.

In the following discussion, we focus on states with $\Omega=\frac{1}{2}$ because, after excitation to the $A\ ^2\Sigma^+_{1/2}$ state, subsequent couplings to states with $\Omega=\frac{3}{2}$ or greater require rotation-induced interactions which will be weak for the conditions of low rotational angular momentum in our experimental study. The $\Omega=\frac{1}{2}$ components of the $X\ ^2\Pi$ and $1\ ^4\Sigma^-$ states exhibit the long-range correlations:

$$X\ ^2\Pi_{1/2} \rightarrow S(^3P_2;m_S=0)+H\left(^2S_{1/2};m_H=\pm\tfrac{1}{2}\right), \quad (15)$$

$$1\ ^4\Sigma^-_{1/2} \rightarrow S(^3P_2;m_S=\pm1)+H\left(^2S_{1/2};m_H=\mp\tfrac{1}{2}\right). \quad (16)$$

Adiabatic dissociation on the $1\ ^4\Sigma^-_{1/2}$ state should thus produce exclusively $S(^3P_2;m_S=\pm1)$ atoms, with mixing at long range with the $X\ ^2\Pi_{1/2}$ state as degeneracy is approached resulting in population of $S(^3P_2;m_S=0)$. There are no routes to formation of $S(^3P_2;m_S=\pm2)$ unless an $\Omega=\frac{3}{2}$

state is populated, but as noted above, this requires (unfavorable) Coriolis interactions. The $\Omega=\frac{3}{2}$ and $\frac{1}{2}$ components of the $1\ ^4\Sigma^-$ state will be effectively mixed by molecular rotation because of the weak coupling of the electron spin to the internuclear axis, giving a possible mechanism for formation of the small fraction of $S(^3P_2)$ $m_S=\pm 2$ atoms suggested by our data analysis. The observed populations of the m levels provide firm evidence for nonadiabatic dynamics between the $1\ ^4\Sigma^-_{1/2}$ and $X\ ^2\Pi_{1/2}$ states which were alluded to in the discussion of spin-orbit branching ratios in Sec. III A.

One $\Omega=\frac{1}{2}$ component of the $1\ ^4\Pi_{1/2}$ state correlates to the $S(^3P_1)+H(^2S_{1/2})$ asymptote (Fig. 5) and was implicated in the production of $S(^3P_1)$ atoms following nonadiabatic transfer of flux from the $1\ ^4\Sigma^-_{1/2}$ state (see Sec. III A). Dissociation on the $1\ ^4\Pi_{1/2}$ state is expected to give rise to $S(^3P_1)$ atoms with $m_S=0$ and mixing with the $1\ ^2\Sigma^-_{1/2}$ state must be invoked to account for the $S(^3P_1, m_s=\pm 1)$ atoms observed experimentally.

Figures 10 and 11 include predictions for m sublevel populations within the approximations of adiabatic and diabatic (or sudden) limits for the dynamics. In the diabatic limit, $m_S=0$ products should dominate the $S(^3P_2)$ channel, with population of $m_S=\pm 1$ a minor pathway. For $S(^3P_1)$ the diabatic model predicts formation of S atoms exclusively with $m_S=\pm 1$. In both cases these predictions are qualitatively (but not quantitatively) reproduced by the experimental data. We thus conclude that the observed dynamical behavior is intermediate between purely diabatic and adiabatic models, which is reinforced by the observed formation of $S(^3P_1)$ and $S(^3P_0)$ photofragments, as discussed in Sec. III A.

IV. CONCLUSIONS

The predissociation dynamics of SH and SD from the $v=0$, 1, and 2 vibrational levels of the $A\ ^2\Sigma^+$ state were investigated by velocity map ion imaging of the $S(^3P_J)$ atom products. The measured spin-orbit branching ratios into $J=0$, 1, and 2 products show that $S(^3P_2)$ atoms are the main product in all cases, with minor branching into $S(^3P_0)$ and $S(^3P_1)$ products. This branching is consistent with predissociation via the $1\ ^4\Sigma^-_{1/2}$ potential which correlates adiabatically to the $S(^3P_2)+H(^2S_{1/2})$ asymptote and is in agreement with deductions from spectroscopic measurements of the $SH(A,v)$ and $SD(A,v)$ lifetimes[19–23] and a model for the predissociation mechanism based on FGR calculations.[21,23] The nonzero population of $S(^3P_0)$ and $S(^3P_1)$ products for predissociation of all vibrational states of $SH(A)$ and $SD(A)$ investigated is indicative of deviations from adiabatic dissociation via the $1\ ^4\Sigma^-_{1/2}$ state, but branching ratios are also inconsistent with a fully diabatic model for dissociation. An intermediate picture thus prevails for the dissociation dynamics following coupling from the $A\ ^2\Sigma^+$ state to the $1\ ^4\Sigma^-_{1/2}$ state in which there are nonadiabatic (spin-orbit mediated) couplings between the $1\ ^4\Sigma^-$ and the $1\ ^4\Pi$ potentials at large internuclear separations (and perhaps also subsequent couplings from the $1\ ^4\Pi$ to the $1\ ^2\Sigma^-$ potential). The evidence from measurements of m sublevel populations for the $S(^3P_2)$ channel also points to nonadiabatic dynamics involving mixing of flux from the $1\ ^4\Sigma^-_{1/2}$ state to the $X\ ^2\Pi_{1/2}$ state. The near absence of $S(^3P_2)$ atoms with $m=\pm 2$ is consistent with weak or negligible Coriolis couplings during the dissociation.

An enhanced branching into $S(^3P_0)$ following excitation to $SH(A,v=2)$ is attributed to the onset of coupling from the $A\ ^2\Sigma^+$ potential to the $1\ ^2\Sigma^-$ potential and subsequent transfer of flux to the $1\ ^4\Pi$ potential which correlates adiabatically to the $S(^3P_0)+H(^2S)$ asymptote. This observation is in accord with the FGR calculations of predissociation rates by Wheeler *et al.*[21] and Brites *et al.*[23] that showed negligible coupling to the $1\ ^2\Sigma^-$ state for $SH(A,v=0,1)$ and $SD(A,v=0-2)$ but an enhancement of this pathway for $SH(A,v=2)$, which was predicted to account for up to 25% of the predissociation mechanism of this vibrational level.

The measured anisotropy parameters β_v show a strong frequency dependence which is well described by calculations, based on the work of Kim *et al.*,[32] that take into account the lifetimes of the excited state levels and interference effects resulting from excitation of the SH or SD molecules via overlapping P, Q, and R branch rotational transition. Evidence is presented that the anisotropy parameters for predissociation of the longer lived SH and SD ($A\ ^2\Sigma^+$) vibrational levels are further reduced by hyperfine interactions, with the coupling of the electronic and rotational angular momenta to the nuclear spin of the H (or D) atom on a time scale of a few nanoseconds partially degrading the prepared optical alignment of the internuclear axes in the excited state.

ACKNOWLEDGMENTS

The Nijmegen group gratefully acknowledges partial financial support by the Council for Chemical Sciences of the Netherlands Organization for Scientific Research, CW-NWO (ECHO Grant No. 700-55-025) and from the Research Training Network Molecular Universe (Grant No. MRTN-CT-2004-512302). We also thank Andre van Roij and Leander Gerritsen for expert technical assistance. The theoretical work has been financially supported by the Council for Chemical Sciences of the Netherlands Organization for Scientific Research (CW-NWO). The Bristol group thanks the University of Bristol for a postgraduate scholarship (R.A.R.) and EPSRC for funding through the LASER Portfolio Partnership Grant No. GR/S71750/01. A.J.O.-E. is grateful to the Royal Society and the Wolfson Foundation for a Research Merit Award.

APPENDIX: FRAGMENT POLARIZATION IN THE ADIABATIC MODEL

The dispersion interaction between two atoms with nonzero angular momentum is discussed in Ref. 55. As the spin-orbit coupling in the H atom is zero, however, we can ignore the H atom electron spin and write the dispersion interaction between $S(^3P_J)$ and $H(^2S_{1/2})$ as a function of the internuclear distance R as[27,56,57]

$$V_{Jm_S}(R) \approx -\frac{C_6(J,m_S)}{R^6}. \tag{A1}$$

The dispersion coefficients $C_6(J,m_S)$ are given by

$$C_6(J,m_S) = C_{6,0}(J) - \frac{3m_S^2 - J(J+1)}{(2J-1)(2J+3)} C_{6,2}(J), \tag{A2}$$

where $C_{6,0}(J)$ and $C_{6,2}(J)$ denote the scalar and rank-2 tensor components of the dispersion interactions, respectively. These two equations show that the energy ordering is determined by $m_S^2 C_{6,2}(J)$. Hence, we must determine the sign of $C_{6,2}(J)$, which is related to the frequency dependent polarizabilities at imaginary frequencies $i\omega$ of the atoms through

$$C_{6,2}(J) = -\frac{3(2J+3)}{2\pi J} \int_0^\infty \alpha_2(J;i\omega)\bar{\alpha}_{\mathrm{H}}(i\omega)d\omega, \tag{A3}$$

where $\alpha_2(J;i\omega)$ is the tensor polarizability of the $\mathrm{S}(^3P_J)$ state and $\bar{\alpha}_{\mathrm{H}}(i\omega)$ is the dynamic polarizability of the $\mathrm{H}(^2S_{1/2})$ atom. As before,[27] we assume that the sign of the integral is minus the sign of $\alpha_2(J;i\omega)$ at $\omega=0$. The polarizability of the fine-structure state is, to a very good approximation, given by[58,57]

$$\alpha_2(J) = (-1)^{S+L+J}(2J+1)\begin{pmatrix} J & 2 & J \\ -J & 0 & J \end{pmatrix}\begin{Bmatrix} L & J & S \\ J & L & 2 \end{Bmatrix} \times \begin{pmatrix} L & 2 & L \\ -L & 0 & L \end{pmatrix}^{-1} \alpha_2(L). \tag{A4}$$

The tensor polarizability $\alpha_2(L)$ is related to the polarizability anisotropy $\Delta\alpha(L,0)$ through[27,56]

$$\alpha_2(L) = -\frac{2}{3}\Delta\alpha(L,0)\frac{L(2L-1)}{L(L+1)}. \tag{A5}$$

Medved *et al.*[59] reported a calculated value for $\mathrm{S}(^3P)$ of $\Delta\alpha(L=1,0)=+4.49$ a.u. Evaluating the 3-j and 6-j symbols for $L=S=1$ in Eq. (A4) gives $\alpha_2(^3P_2)=\alpha_2(L=1)<0$ and $\alpha_2(^3P_1)=-0.5\alpha_2(L=1)>0$. This gives a positive anisotropic dispersion coefficient $C_{6,2}(J=2)>0$ and hence $m_S=0$ is the lowest for the $J=2$ fine-structure state, while $m_S=0$ is the upper level for $J=1$.

[1] G. G. Balint-Kurti, A. J. Orr-Ewing, A. Brown, J. A. Beswick, and O. S. Vasyutinskii, J. Chem. Phys. **116**, 10760 (2002).
[2] A. Brown, G. G. Balint-Kurti, and O. S. Vasyutinskii, J. Phys. Chem. A **108**, 7790 (2004).
[3] M. N. R. Ashfold, N. H. Nahler, A. J. Orr-Ewing, O. P. J. Vieuxmaire, R. L. Toomes, T. N. Kitsopoulos, I. A. Garcia, D. A. Chestakov, S. M. Wu, and D. H. Parker, Phys. Chem. Chem. Phys. **8**, 26 (2006).
[4] A. G. Smolin, O. S. Vasyutinskii, and A. J. Orr-Ewing, Mol. Phys. **105**, 885 (2007).
[5] A. G. Suits and O. S. Vasyutinskii, Chem. Rev. (Washington, D.C.) **108**, 3706 (2008).
[6] R. Schinke, *Photodissociation Dynamics* (Cambridge University Press, Cambridge, 1995).
[7] S. Lee and K. F. Freed, J. Chem. Phys. **87**, 5772 (1987).
[8] S. Lee, C. J. Williams, and K. F. Freed, Chem. Phys. Lett. **130**, 271 (1986).
[9] D. R. Yarkony, J. Chem. Phys. **97**, 1838 (1992).
[10] G. Parlant and D. R. Yarkony, J. Chem. Phys. **110**, 363 (1999).
[11] S. Lee, H. Sun, B. Kim, and K. F. Freed, J. Chem. Phys. **114**, 5537 (2001).
[12] A. D. Webb, N. H. Nahler, R. N. Dixon, and M. N. R. Ashfold, J. Chem. Phys. **125**, 204312 (2006).
[13] D. C. Radenovic, A. J. A. van Roij, D. A. Chestakov, A. Eppink, J. J. ter Meulen, D. H. Parker, M. P. J. van der Loo, G. C. Groenenboom, M. E. Greenslade, and M. I. Lester, J. Chem. Phys. **119**, 9341 (2003).
[14] D. C. Radenovic, A. J. A. van Roij, S. M. Wu, J. J. ter Meulen, D. H. Parker, M. P. J. van der Loo, L. M. C. Janssen, and G. C. Groenenboom, Mol. Phys. **106**, 557 (2008).
[15] W. Zhou, Y. Yuan, and J. Zhang, J. Chem. Phys. **119**, 9989 (2003).
[16] J. W. Johns and D. A. Ramsay, Can. J. Phys. **39**, 210 (1961).
[17] D. A. Ramsay, J. Chem. Phys. **20**, 1920 (1952).
[18] W. Ubachs, J. J. ter Meulen, and A. Dymanus, Chem. Phys. Lett. **101**, 1 (1983).
[19] W. Ubachs and J. J. ter Meulen, J. Chem. Phys. **92**, 2121 (1990).
[20] M. Kawasaki, H. Sato, G. Inoue, and M. Suzuki, J. Chem. Phys. **91**, 6758 (1989).
[21] M. D. Wheeler, A. J. Orr-Ewing, and M. N. R. Ashfold, J. Chem. Phys. **107**, 7591 (1997).
[22] M. D. Wheeler, A. J. Orr-Ewing, M. N. R. Ashfold, and T. Ishiwata, Chem. Phys. Lett. **268**, 421 (1997).
[23] V. Brites, D. Hammoutene, and M. Hochlaf, J. Phys. B **41**, 045101 (2008).
[24] M. R. Manaa, Int. J. Quantum Chem., Quantum Chem. Symp. **56**, 577 (1995).
[25] W. D. Zhou, Y. Yuan, S. P. Chen, and J. S. Zhang, J. Chem. Phys. **123**, 054330 (2005).
[26] J. Dillon and D. Yarkony, personal communication (2008).
[27] L. M. C. Janssen, M. P. J. van der Loo, G. C. Groenenboom, S. M. Wu, D. C. Radenovic, A. J. A. van Roij, I. A. Garcia, and D. H. Parker, J. Chem. Phys. **126**, 094304 (2007).
[28] R. E. Continetti, B. A. Balko, and Y. T. Lee, Chem. Phys. Lett. **182**, 400 (1991).
[29] C. W. Hsu, C. L. Liao, Z. X. Ma, P. J. H. Tjossem, and C. Y. Ng, Chem. Phys. Lett. **199**, 78 (1992).
[30] G. P. Morley, I. R. Lambert, D. H. Mordaunt, S. H. S. Wilson, M. N. R. Ashfold, R. N. Dixon, and C. M. Western, J. Chem. Soc., Faraday Trans. **89**, 3865 (1993).
[31] S. H. S. Wilson, J. D. Howe, and M. N. R. Ashfold, Mol. Phys. **88**, 841 (1996).
[32] H. Kim, K. S. Dooley, S. W. North, G. E. Hall, and P. L. Houston, J. Chem. Phys. **125**, 133316 (2006).
[33] V. V. Kuznetsov and O. S. Vasyutinskii, J. Chem. Phys. **127**, 044308 (2007).
[34] P. L. Houston, A computer program that calculates beta and absorption intensity as a function of wave number and broadening parameters (http://people.ccmr.cornell.edu/~plh2/group/Betaofnu.htm).
[35] M. E. Greenslade, M. I. Lester, D. C. Radenovic, A. J. A. van Roij, and D. H. Parker, J. Chem. Phys. **123**, 074309 (2005).
[36] M. C. Van Beek and J. J. ter Meulen, Chem. Phys. Lett. **337**, 237 (2001).
[37] M. N. R. Ashfold, B. Tutcher, and C. M. Western, Mol. Phys. **66**, 981 (1989).
[38] K. Schreel, J. Schleipen, A. Eppink, and J. J. ter Meulen, J. Chem. Phys. **99**, 8713 (1993).
[39] NIST Atomic Spectra Database, Version 3, 2005 (http://physics.nist.gov/PhysRefData/ASD/index.html).
[40] C.-W. Hsu, C.-L. Liao, Z.-L. Ma, P. J. H. Tjossem, and C. Y. Ng, J. Chem. Phys. **97**, 6283 (1992).
[41] M. Brouard, F. Quadrini, and C. Vallance, J. Chem. Phys. **127**, 084305 (2007).
[42] H. Lefebvre-Brion and R. W. Field, *The Spectra and Dynamics of Diatomic Molecules* (Elsevier, New York, 2004).
[43] R. N. Zare and D. R. Herschbach, Proc. IEEE **51**, 173 (1963).
[44] A. M. Coroiu, D. H. Parker, G. C. Groenenboom, J. Barr, I. T. Novalbos, and B. J. Whitaker, Eur. Phys. J. D **38**, 151 (2006).
[45] Y. Mo, H. Katayanagi, M. C. Heaven, and T. Suzuki, Phys. Rev. Lett. **77**, 830 (1996).
[46] Y. Mo and T. Suzuki, J. Chem. Phys. **109**, 4691 (1998).
[47] C. M. Western, PGOPHER, a program for simulating rotational structure (http://pgopher.chm.bris.ac.uk).
[48] L. Meerts, personal communication (2008).
[49] D. Sofikitis, L. Rubio-Lago, M. R. Martin, D. J. Ankeny Brown, N. C. M. Bartlett, A. J. Alexander, R. N. Zare, and P. T. Rakitzis, J. Chem. Phys. **127**, 144307 (2007).
[50] A. J. Orr-Ewing and R. N. Zare, Annu. Rev. Phys. Chem. **45**, 315 (1994).
[51] R. N. Zare, *Angular Momentum* (Wiley, New York, 1988).
[52] R. Altkorn, R. N. Zare, and C. H. Greene, Mol. Phys. **55**, 1 (1985).
[53] J. Zhang, C. W. Riehn, M. Dulligan, and C. Wittig, J. Chem. Phys. **104**, 7027 (1996).

[54] R. N. Zare, Ber. Bunsenges. Phys. Chem **86**, 422 (1982).
[55] G. C. Groenenboom, X. Chu, and R. V. Krems, J. Chem. Phys. **126**, 204306 (2007).
[56] X. Chu, A. Dalgarno, and G. C. Groenenboom, Phys. Rev. A **72**, 032703 (2005).
[57] J. R. P. Angel and P. G. H. Sanders, Proc. R. Soc. London, Ser. A **305**, 125 (1968).
[58] X. Chu, A. Dalgarno, and G. C. Groenenboom, Phys. Rev. A **75**, 032723 (2007).
[59] M. Medved, P. W. Fowler, and J. M. Hutson, Mol. Phys. **98**, 453 (2000).